NATURAL HAZARDS

The complex dynamics of the 2023 Kahramanmaraş, Turkey, M_w 7.8-7.7 earthquake doublet

Zhe Jia[1]*, Zeyu Jin[1], Mathilde Marchandon[2], Thomas Ulrich[2], Alice-Agnes Gabriel[1,2], Wenyuan Fan[1], Peter Shearer[1], Xiaoyu Zou[1], John Rekoske[1], Fatih Bulut[3], Aslı Garagon[3], Yuri Fialko[1]

The destructive 2023 moment magnitude (M_w) 7.8-7.7 earthquake doublet ruptured multiple segments of the East Anatolian Fault system in Turkey. We integrated multiscale seismic and space-geodetic observations with multifault kinematic inversions and dynamic rupture modeling to unravel the events' complex rupture history and stress-mediated fault interactions. Our analysis reveals three subshear slip episodes during the initial M_w 7.8 earthquake with a delayed rupture initiation to the southwest. The M_w 7.7 event occurred 9 hours later with a larger slip and supershear rupture on its western branch. Mechanically consistent dynamic models accounting for fault interactions can explain the unexpected rupture paths and require a heterogeneous background stress. Our results highlight the importance of combining near- and far-field observations with data-driven and physics-based models for seismic hazard assessment.

The moment magnitude (M_w) 7.8 and 7.7 Kahramanmaraş earthquakes in Turkey on 6 February 2023 caused enormous destruction and tens of thousands of casualties from collapsed structures and together were one of the deadliest natural disasters for Turkey and Syria over the past millennium (*1*). The Kahramanmaraş sequence is the first great earthquake doublet with a combined moment magnitude of 8 recorded in a continental strike-slip fault system. Unlike regular aftershocks that are more than one order of magnitude smaller than their mainshock, doublet events pose a greater hazard because they can cause more severe damage by striking already weakened buildings and structures. We show that the Kahramanmaraş earthquake doublet involved a remarkable sequence of subevents that occurred with varying rupture velocities, geometries, and time delays on branched fault segments, which challenge our understanding of earthquake interactions and the dynamics of rupture propagation.

Seismologists commonly approximate earthquakes as point sources or as slip along a single fault with fixed rupture velocity. However, large earthquakes often rupture multiple fault segments within a complex network (*2*–*6*). Occasionally, events of a comparable magnitude occur within minutes to hours of the initial event, resulting in earthquake doublets (*7*–*9*). Branching faults may further complicate rupture dynamics (*10*–*12*). Whether rupture stops or continues propagating at fault junctions can determine earthquakes' eventual size and destructive potential (*13*). When applied to complex ruptures on multiple faults, conventional earthquake source imaging often involves oversimplified assumptions, yielding stark differences in source models and their interpretations (*14*, *15*). Initial studies of the Kahramanmaraş earthquakes presented a wide range of earthquake models and interpretations (*16*–*21*), likely from focusing on particular datasets and aspects of the rupture process. These differences motivate unified and self-consistent approaches that integrate diverse datasets with state-of-the-art rupture models to advance our understanding of the earthquake dynamics.

We performed a comprehensive investigation of the M_w 7.8-7.7 Kahramanmaraş doublet using data-driven and physics-based analyses applied to near- and far-field seismic and geodetic observations. Our results reveal that the earthquakes followed unexpected rupture trajectories, which included delayed backward branching, statically and dynamically aided triggering, and a combination of subshear and supershear rupture episodes. These discoveries call for reevaluating the role of cascading failure mechanisms when assessing the destructive potential of large earthquakes within complex fault networks.

The geometrically complex M_w 7.8-7.7 earthquake doublet

On 6 February 2023, two major (M_w > 7) earthquakes ruptured several previously recognized fault systems within 9 hours (Fig. 1). The East Anatolian Fault (EAF) is a mature transform fault accommodating up to 10 mm/year of left-lateral motion between the Arabian and Anatolian plates (Fig. 1) (*22*). Several M_w ~7 earthquakes occurred on the EAF historically, but none ruptured the entire southern section of the EAF (*23*). The estimated dimensions of the historic events suggest that geometric complexities such as fault bends and step-overs may have controlled the event sizes (*23*, *24*). The second earthquake (M_w 7.7) occurred on the Savrun-Çardak Fault (SCF), extending ~150 km along the east-west direction (Fig. 1). The SCF has been relatively quiescent, with only two moderate (M_w <6) events recorded in the past 100 years (*25*).

We constrained the rupture geometry on the basis of surface traces mapped using Synthetic Aperture Radar data (*26*) and precisely relocated aftershocks (*27*, *28*). We found that the Kahramanmaraş doublet ruptured at least six major fault segments (Fig. 1). The epicenter of the M_w 7.8 earthquake is located on a subsidiary fault, the Nurdağı-Pazarcık (Narlı) Fault (NPF) (Fig. 1A, fault 1) (*20*), from which the rupture propagated to the EAF, and then ruptured along the EAF to both the northeast and southwest (Fig. 1A, faults 2 and 3), for a total length of about 300 km. Unlike the historical M_w ~7 events, the M_w 7.8 earthquake propagated across at least four possible geometric barriers, including fault bends and stepovers.

The static slip distribution (Fig. 1B) obtained from inversions of Synthetic Aperture Radar (SAR) and Global Navigation Satellite System (GNSS) data (figs. S1 to S7) shows that the largest slip in the M_w 7.8 event is on the EAF at its junction with the NPF, near the towns of Kahramanmaraş and Pazarcık, with a peak slip in excess of 8 m. Most of the coseismic slip is in the upper 20 km of the seismogenic layer (Fig. 1B). Slip at the surface is highly heterogeneous, which is consistent with field observations (*18*), but on average increases from the southwest to the northeast ends of the M_w 7.8 rupture (fig. S8). The area of substantial slip extends to the northeast from the junction for about 150 km to the western tip of the 2020 M_w 6.7 Elazığ rupture (Fig. 1A) (*29*). South of the junction, the M_w 7.8 rupture extends to the southern end of the EAF. The average coseismic slip on the southwest branch of the M_w 7.8 rupture is smaller than the average slip on the northeast branch (Fig. 1B and fig. S2).

We resolved the spatiotemporal rupture process with a subevent inversion method by using both near- and far-field seismic observations (*30*, *31*). The M_w 7.8 earthquake had six subevents that altogether spanned ~90 s (Fig. 2A). The M_w 6.8 subevent E1 that ruptured the NPF was followed 18 s later by the largest subevent E2 (M_w 7.5) at the NPF-EAF intersection. The earthquake then ruptured northeastward along the EAF for about 130 km (M_w 7.5 subevent E3), as well as, after a short delay, backward from the NPF junction for about 150 km along the southwestern segment of the EAF, with an integrated slip equivalent to a M_w 7.4 earthquake (subevents E4 to E6). Teleseismic *P* wave back-projection (*32*) confirmed the rupture process, with imaged high-frequency radiation peaks outlining the major subevents (Fig. 2A) and indicating an average

[1]Scripps Institution of Oceanography, University of California, San Diego, La Jolla, CA 92093, USA. [2]Department of Earth and Environmental Sciences, Ludwig-Maximilians-Universität München, 80539 Munich, Germany. [3]Geodesy Department, Bogazici University Kandilli Observatory and Earthquake Research Institute, Istanbul 34342, Turkey.
*Corresponding author. Email: z5jia@ucsd.edu

rupture velocity of 3 km/s. To further constrain the slip history, we performed a joint kinematic slip inversion of the M_w 7.8 earthquake constrained by far- and near-field seismic and geodetic data (*26*, *33*). Our kinematic inversion results agree with the static and subevent models (Fig. 2B). The best-fit kinematic slip model images 10-s-delayed backward branching at the NPF-EAF intersection, toward the southwest (Fig. 2B), constrained by the strong-motion data (fig. S17). It also indicates average rupture velocities of 3.2 km/s and 2.8 km/s for the northeastern and southwestern branches, respectively (fig. S18). Tracking ground motion pulses at near-fault strong

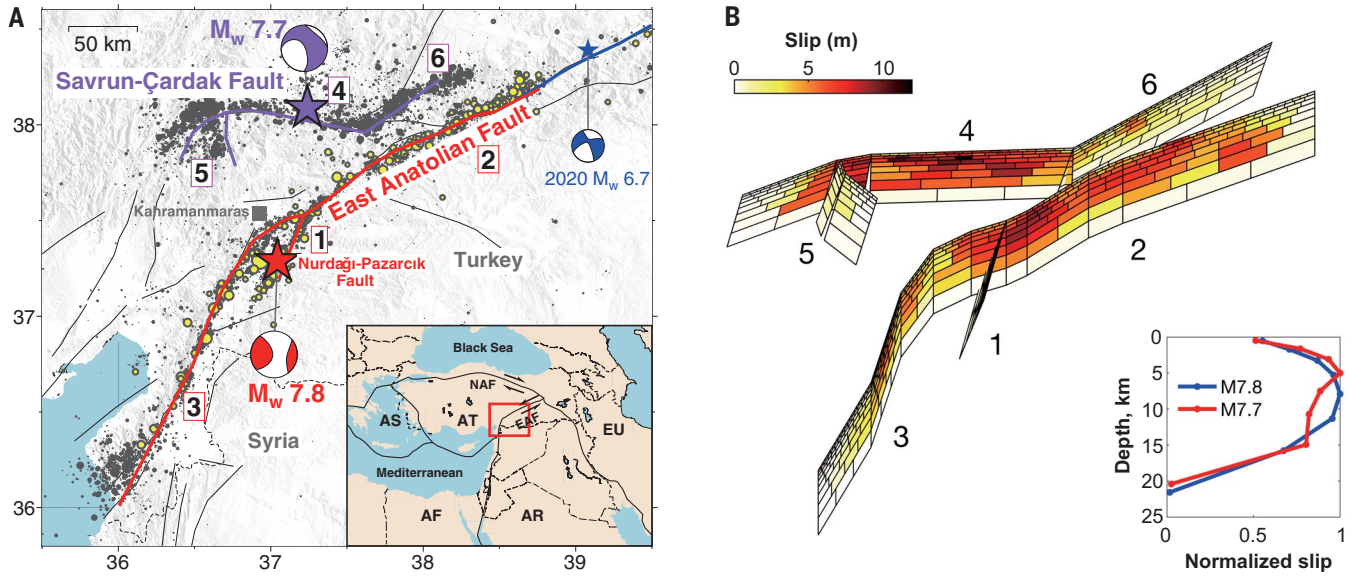

Fig. 1. A multifault earthquake doublet. (**A**) Tectonic background and aftershock seismicity of the study area near Kahramanmaraş, Turkey. Red and purple stars indicate the M_w 7.8 and 7.7 earthquake epicenters according to the Turkey Disaster and Emergency Management Authority (*53*), and red and purple beachballs indicate focal mechanisms from the Global Centroid Moment Tensor catalog, respectively. Red and purple lines indicate surface ruptures identified from SAR data (*26*). Yellow dots indicate aftershocks for the period between the M_w 7.8 and 7.7 earthquakes, and black dots indicate aftershocks after the M_w 7.7 event (*28*). The blue line and blue beachball denote the rupture extent and focal mechanism of the 2020 M_w 6.7 Elazığ earthquake (*29*). (Inset) The regional tectonics and major plate boundary faults (solid black lines). Red outline denotes the study area. (**B**) Finite-fault model of the 2023 doublet derived from inversions of space geodetic (InSAR and GNSS) data. Fault segment numbers correspond to those shown in (A), in order of their rupture time: 1, Nurdağı-Pazarcık Fault; 2 and 3; East Anatolian Fault; 4 to 6, Savrun-Çardak Fault. (Inset) The along-strike averaged coseismic slip normalized by the maximum slip amplitude, as a function of depth (*49*).

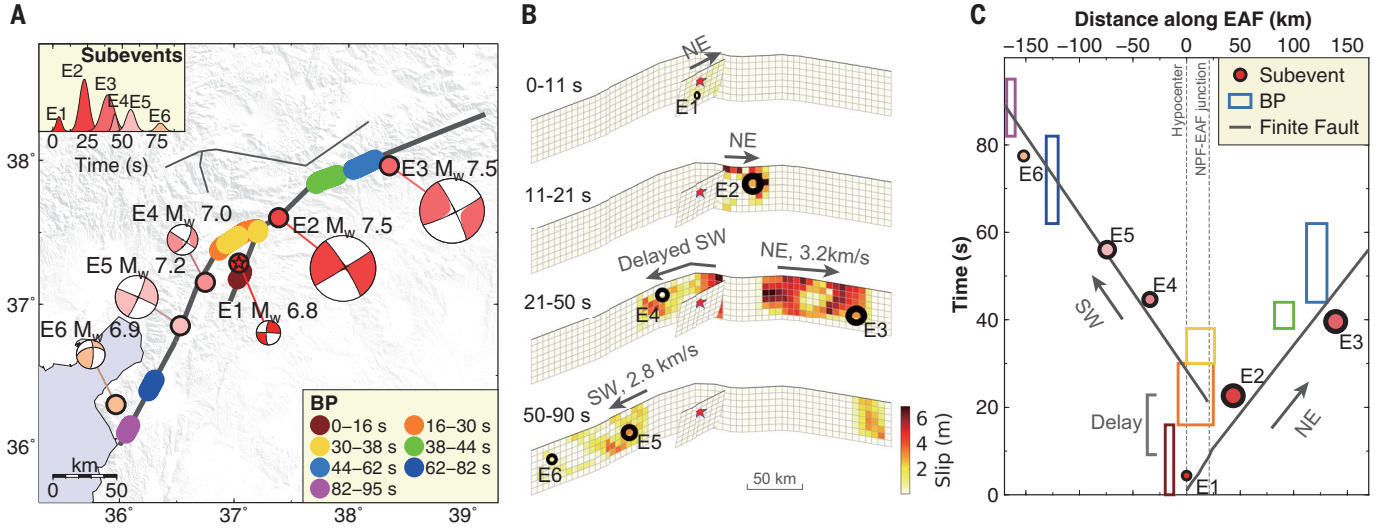

Fig. 2. Complex slip evolution of the M_w 7.8 earthquake, including delayed initiation of slip. (**A**) Subevent model from near- and far-field seismic observations and back-projection results, suggesting that the M_w 7.8 earthquake initiated on the NPF-1 (Fig. 1B, fault 1), then propagated bilaterally, northeast along the EAF-2 (Fig. 1B, fault 2) and southwest along the EAF-3 (Fig. 1B, fault 3). The rupture of fault 2 terminates around 50 s, whereas rupture of fault 3 continues for an additional 30 s. (**B**) Rupture history within different time intervals from our kinematic slip inversion of far- and near-field seismic and geodetic data. We infer rupture velocities of 3.2 and 2.8 km/s for the northeast and southwest episodes, respectively, and a 10-s delay in the onset of the southwest rupture along EAF-3 with respect to the NE rupture along EAF-2. The slip distribution within each time interval agrees with the subevent (black circles) inversion. (**C**) Subevents, back-projection locations and times, and finite-fault velocities [in (B)] consistently indicate delayed initiation of slip on branch EAF-3.

motion stations along the southwestern segment also yielded a rupture velocity of ~3 km/s (fig. S18), confirming an overall subshear nature. All our kinematic models consistently reveal a ~300-km-long complex bilateral multisegment rupture, subshear rupture velocities, and delayed triggering of the southwest segment of the M_w 7.8 event (Fig. 2C).

The subsequent M_w 7.7 earthquake ruptured a 150-km-long section of the west-trending SCF, within 90 km of the M_w 7.8 earthquake hypocenter. The aftershock distribution and surface offsets indicate branching and abrupt changes in strike at both the eastern and western ends of the M_w 7.7 rupture (Fig. 1). Geodetic data and our associated static slip model (Fig. 1B) suggest rupture along an 80-km-long segment of the SCF system (Fig. 1, faults 4 and 5), but not along the eastern end of the Sürgü fault that connects to the EAF. Instead, the M_w 7.7 rupture diverted sharply onto the Doğanşehir branch, which angles to the northeast (Fig. 1, fault 6). The M_w 7.7 event shows a concentrated slip distribution with >10 m peak slip around its hypocenter, suggesting a substantially higher stress drop than that of the initial M_w 7.8 earthquake, which spread a lower-amplitude slip over a larger region.

Our analysis of the rupture history of the M_w 7.7 event identified four major subevents, lasting for about 30 s (Fig. 3A). The first three subevents, E1 to E3, all cluster near the epicenter and account for more than 80% of the total seismic moment, suggesting a compact bilateral rupture in the central SCF. The focal mechanism (strike of 237°) and location of the last subevent (E4; M_w 7.1) agree with the static slip model on the Doğanşehir branch (Fig. 1B). All subevents of both earthquakes have almost pure double-couple mechanisms (Figs. 2A and 3A), suggesting that the strong non–double-couple components in the Global Centroid-Moment-Tensor solutions (Fig. 1A) (*34*) are due to highly variable rupture geometries. The overall shorter duration and smaller rupture extent of the M_w 7.7 event make back-projection analysis less effective for resolving rupture details, but our kinematic finite-slip inversion can still be applied.

The kinematic finite-fault model of the M_w 7.7 earthquake also indicates a compact slip distribution. In addition, it indicates a westward rupture velocity of ~4.5 km/s (Fig. 3B), exceeding the shear-wave speed in the crust. The waveforms recorded at the westward seismic stations strongly constrain this supershear rupture episode (Fig. 3C and fig. S19), which is consistent with analysis of high-rate GNSS data (*20*). By contrast, the eastward rupture likely propagated at a slower velocity of 2.5 km/s. The intriguing supershear rupture episode may imply locally higher prestress (*35*) and high stress drop (*36*) as in our dynamic rupture models.

Dynamics, triggering, and stress interaction of the doublet

Dynamic rupture modeling involves simulating how earthquakes nucleate, propagate, and arrest. Unlike purely data-driven kinematic slip inversions, such models predict the evolution of slip, seismic waves, and surface deformation in a physically self-consistent manner. Detailed, physics-based interpretations can help verify whether inferred rupture scenarios are mechanically plausible but are computationally challenging and typically take years to develop [for example, (*10*, *12*, *13*)].

We present data-informed dynamic rupture simulations of the 2023 Kahramanmaraş earthquakes that illuminate complex details of the rupture process. Our three-dimensional (3D) dynamic rupture models include stress changes computed from the slip distribution of the static slip model (*37*), large-scale variability in fault loading inferred from regional seismotectonics, and the relative effects of the static and dynamic stresses of the M_w 7.8 event on the faults hosting the second earthquake (fig. S20) (*26*). The dynamic rupture models independently reproduce the main features of the kinematic models (Fig. 4 and fig. S21), providing a physics-based validation of the inferred rupture histories.

Our forward simulations use the complex fault geometries of both earthquakes informed from geodetic analysis (Fig. 1) to spontaneously replicate the moment rate release, magnitude, rupture velocity and delays, as well as the lack of instantaneous dynamic triggering of the M_w 7.7 event. The dynamic rupture synthetics produce surface displacements and slip histories that compare well with the high-resolution geodetic data (fig. S22), kinematic rupture

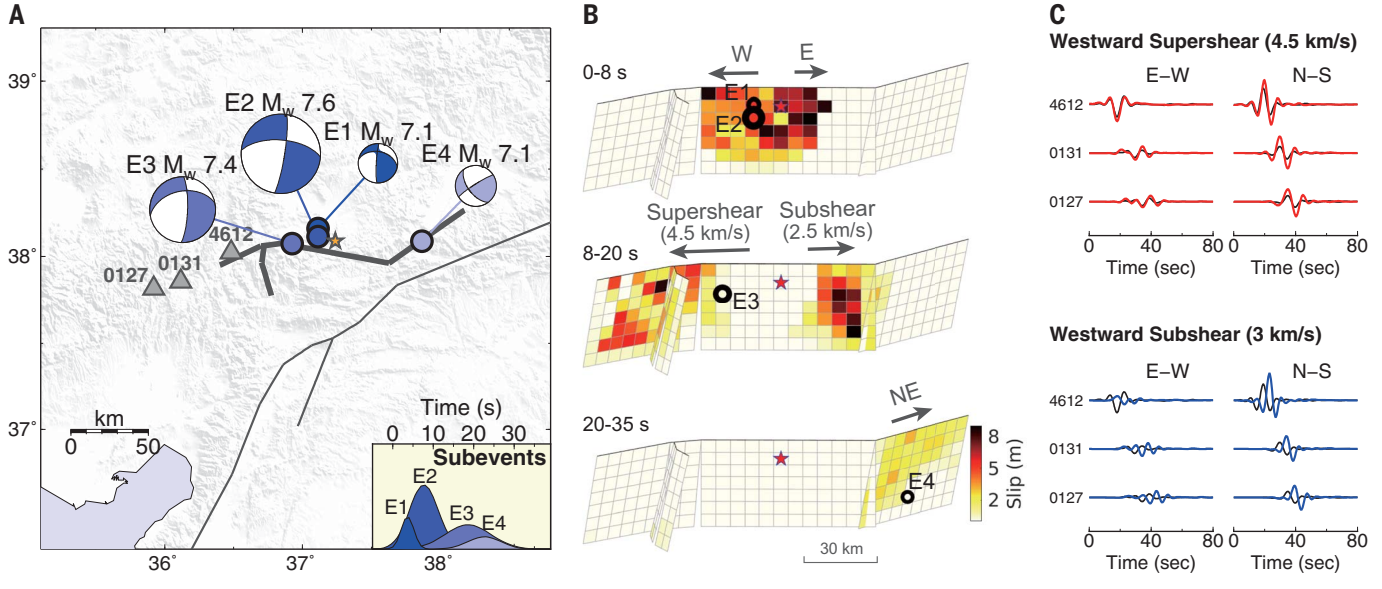

Fig. 3. Asymmetric kinematics of the M_w 7.7 earthquake. (**A**) Three subevents close to the hypocenter suggest a bilateral rupture. The fourth event images the rupture of the Doğanşehir branch (Fig. 1B, fault 6). (**B**) Asymmetric bilateral rupture velocities of the M_w 7.7 event. The westward rupture has an inferred supershear velocity of 4.5 km/s, whereas a subshear velocity is seen toward the east (2.5 km/s). Subevent locations are based on their seismic moment centroids. The slip may not be the largest at the centroid location, specifically for bilateral ruptures. For example, E3 (10 to 30 s) averages slip pulses of both the westward supershear and the eastward subshear rupture. (**C**) A westward supershear rupture velocity (red waveforms) better explains observed waveforms (black) at near-fault strong motion stations to the west [triangles in (A)] than a subshear rupture (blue).

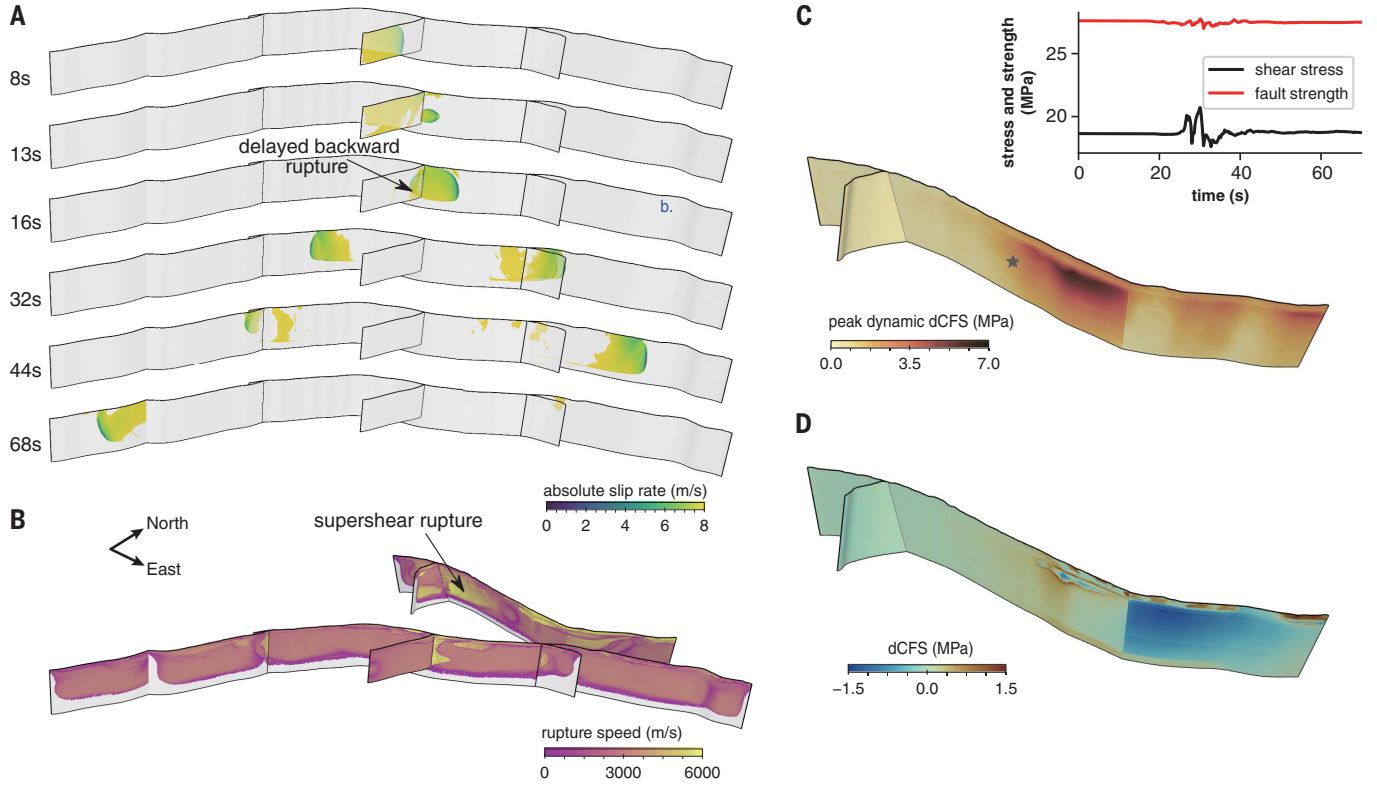

Fig. 4. 3D dynamic rupture scenarios and stress-mediated interactions of the M_w 7.8 and 7.7 earthquakes. (**A**) Snapshots of absolute slip rate evolution in the M_w 7.8 dynamic rupture scenario (movie S1). (**B**) Modeled rupture speeds in linked dynamic rupture simulations (*54*) of both earthquakes indicating dominantly subshear rupture speeds but sustained westward supershear during the M_w 7.7 scenario (fig. S21 and movie S2). (**C**) Peak absolute dynamic shear stress perturbation reaching up to 7 MPa measured in the direction of maximum initial traction. (Inset) Evolution of dynamic shear stress and fault strength at the M_w 7.7 hypocenter (black star). (**D**) Static Coulomb failure stress changes (ΔCFS) assuming a static friction coefficient of 0.6.

representations (Fig. 4 and fig. S21), and observed ground motions (Fig. 5 and figs. S23 to S25). The modeled M_w 7.8 earthquake dynamics are illustrated in Fig. 4A. The NPF-EAF intersection slows subshear rupture on the NPF that then branches with dynamically favorable forward directivity (*38*) northeastward along the EAF. The large fault branching angle poses a strong dynamic barrier in backward-directivity (*39*), leading to substantially delayed EAF rupture toward the southwest. Continuous dynamic unclamping, transient shear stressing, and static stress buildup at the fault intersection due to the unilaterally propagating northeast rupture allowed the rupture to eventually fracture the EAF bilaterally (fig. S26). Rupture speed remained overall subshear during the earthquake (Fig. 4B).

Dynamic rupture modeling of the M_w 7.7 earthquake features bilateral rupture with unequal rupture speeds, confirming dominant supershear westward and subshear eastward propagation. Our M_w 7.8 dynamic rupture model predicts a highly variable pattern of static and dynamic stresses resolved on the faults that hosted the M_w 7.7 earthquake (Fig. 4, C and D). The hypocentral area of the M_w 7.7 event experienced an increase in static Coulomb stress of several hundred kilopascals because of the M_w 7.8 earthquake, resulting from both an increase in shear stress and a decrease in fault-normal compression (fig. S27). It also experienced a much larger transient increase in the Coulomb stress of a few megapascals owing to passing seismic waves (Fig. 4C), which nevertheless did not result in instantaneous triggering.

Discussion and conclusions

Our analyses reveal unexpected rupture paths. The Kahramanmaraş doublet originated as a moderate event on the NPF branch fault with a magnitude of only 6.8, yet the rupture was able to successfully cross the junction of the NPF and EAF, which would usually be considered a geometric barrier that conditionally gates the rupture propagation (*40*, *41*). As a result, the earthquake intensified with the northeastward propagation along the EAF then dynamically triggered backward rupture toward the southwest by continuously unclamping and stressing from the forward branch, eventually culminating in a M_w 7.8 event, with total seismic moment increased by a factor of 30 compared with the initial rupture on the NPF. In addition, the M_w 7.8 earthquake increased the Coulomb stress on the central part of the SCF, which may have aided the nucleation of the M_w 7.7 earthquake 9 hours later. The entire process highlights the additional hazard brought by rupture triggering across a network of faults, challenging earthquake hazard assessments that typically do not consider such multifault-triggering scenarios.

The M_w 7.8 earthquake involved backward fault branching, which is highly unfavorable from a dynamic perspective, thus commonly neglected in hazard studies. Several previous continental earthquakes—including the 1992 Landers, the 1999 Hector Mine, and the 2002 Denali earthquakes—have also exhibited localized backward branching (*10*). Existing explanations of this phenomenon include backward rupture jumping induced by sudden rupture arresting or nonuniform prestress fields caused by earthquake cycles (*39*, *42*). Our dynamic rupture models indicate that backward branching during the M_w 7.8 event does not necessarily require a complex arrangement of the receiver fault (*42*) or triggering of supershear rupture (*43*). Instead, the progressive build-up of slip on

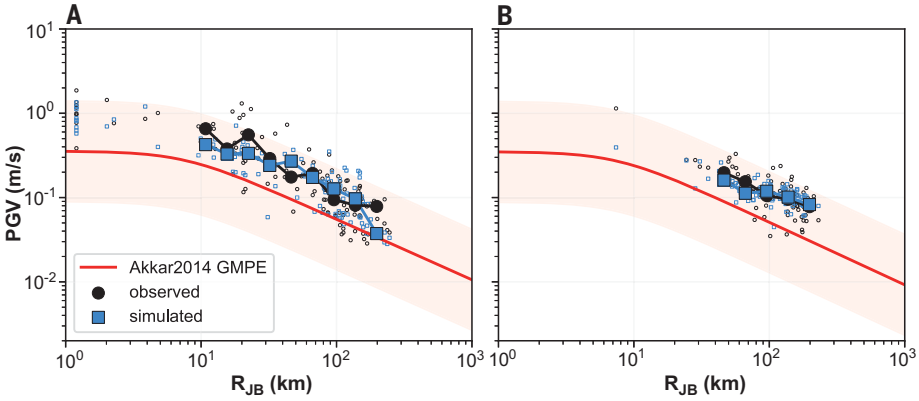

Fig. 5. Peak ground velocities (PGVs) plotted against Joyner-Boore distance (R_{JB}) for the M_w 7.8 and M_w 7.7 earthquakes. (A) The M_w 7.8 earthquake. (B) The M_w 7.7 earthquake. Observed PGVs from strong motion accelerometers are indicated with open black circles, and simulated PGVs from the dynamic rupture simulations are indicated with open blue squares. We bin the PGV data by R_{JB} and plot the medians for each distance bin (solid markers). The red curve indicates PGV predicted by a ground motion model (*55*), assuming an average shear wave velocity for the top 30 m of soil (VS_{30}) of 760 m/s, with the shaded area denoting its uncertainty. All PGV are rotationally independent geometric mean values (GMRotD50). We include simulated and observed data at the same locations, respectively.

the forward branch of the EAF continuously unclamps and stresses the backward branch of the EAF, eventually leading to a delayed and self-sustained branching toward the southwest, which is a simple yet effective mechanism.

One of the unexpected aspects of the M_w 7.7 earthquake is that it did not rupture through the eastern Sürgü segment and arrive at the EAF, contrary to earlier suggestions (*20*), but instead deviated to the Doğanşehir branch. The Interferometric Synthetic Aperture Radar (InSAR), aftershock, and seismic data clearly show such a deviation (figs. S1 and S14). The straightforward rupture path along the Sürgü fault was encouraged by the static stress changes from the M_w 7.8 event (fig. S27), unlike the sharp deviation to the Doğanşehir fault, which was actually unloaded by the M_w 7.8 event (Fig. 4D and movie S3). Possible explanations, which may be tested by future geodetic and seismological observations, include velocity-strengthening behavior of the eastern Sürgü segment or local stress heterogeneity, for example, because of past earthquakes (*44*). Considerable regional stress heterogeneity, as is required by our dynamic rupture models (fig. S20), is implied by extremely complex rupture geometries that involve changes in the strike angle of up to 90° (Fig. 1 and fig. S27) (*45*). Some faults in the study area, including the EAF, exhibit shallow creep (*46*); however, creep has to be pervasive to potentially suppress an incoming dynamic rupture. Observations spanning all phases of the earthquake cycle are needed to constrain the velocity- and depth-dependent frictional properties of active faults (*47*, *48*). Shallow creep might be responsible for a substantial reduction in the amplitude of coseismic slip in the top few kilometers of the upper crust (Fig. 1B), which is well resolved in our inverse models (fig. S28). Subsequent observations will show whether this reduction can be compensated by shallow afterslip or constitutes a long-term shallow slip deficit (*49*), implying widespread off-fault yielding (*47*, *50*).

We also found intriguing variations in rupture velocity across segments of the EAF-SCF fault network. Although the M_w 7.8 event produced extreme shaking with peak ground accelerations (PGAs) exceeding 1 g for near-fault stations, the observed and simulated M_w 7.7 ground motions are similar or larger when compared at the same distance (Fig. 5 and figs. S23 and S24), which is consistent with a potentially larger stress drop of the M_w 7.7 event. The modeled and observed M_w 7.7 event shaking shows less distance dependence, which may be due to the effects of supershear rupture.

The western branch of the SCF experienced a supershear rupture episode, whereas the eastern SCF branch and the EAF hosted subshear ruptures with considerable delays. In general, our modeling shows that the pre-event stress heterogeneities, dynamic and static redistribution of stress, and the geometry of the faults may control these diverse rupture characteristics.

The Kahramanmaraş doublet ruptured multiple faults in distinct slip episodes, likely involving complex stress-triggering processes across different temporal and spatial scales. Such processes resulted in the increased rupture length and seismic moment of the Turkey earthquake doublet, and a substantially larger destructive potential compared with the "typical" M_w ~7 historical earthquakes in the region (*23*). Such a variability might be interpreted in terms of the supercycle model (*51*). By using integrated methods that combine near- and far-field seismic and geodetic observations and investigating data-derived models and physics-based rupture simulations, we show that stress interactions and static and dynamic triggering worked together across a complex fault system, resulting in a cascade of rupture with a larger than usual total rupture length and moment magnitude. Our study shows that complementary data-driven and physics-based analyses, which in isolation often lead to nonunique or even contradictory results, can jointly and efficiently unravel highly complex earthquake dynamics based on dense near-field observations. The unusual static and dynamic interactions during and between the events of the Kahramanmaraş doublet call for reassessment of common assumptions built into seismic hazard assessments.

REFERENCES AND NOTES

1. M. Edrik, M. B. D. Tümsa, A. Pınar, E. Altunel, A. C. Zülfikar, "A preliminary report on the February 6, 2023 earthquakes in Türkiye" (Temblor, 2023).
2. T. Lay, L. Ye, Y. Bai, K. F. Cheung, H. Kanamori, *Geophys. Res. Lett.* **45**, 9542–9551 (2018).
3. L. Meng *et al.*, *Science* **337**, 724–726 (2012).
4. E. Hauksson, L. M. Jones, K. Hutton, *Bull. Seismol. Soc. Am.* **92**, 1154–1170 (2002).
5. E. Hauksson, L. M. Jones, K. Hutton, D. Eberhart-Phillips, *J. Geophys. Res.* **98** (B11), 19835–19858 (1993).
6. Z. E. Ross *et al.*, *Science* **366**, 346–351 (2019).
7. A. Ghods *et al.*, *Geophys. J. Int.* **203**, 522–540 (2015).
8. C. J. Ammon, H. Kanamori, T. Lay, *Nature* **451**, 561–565 (2008).
9. W. Fan, P. M. Shearer, *Science* **353**, 1133–1136 (2016).
10. D. D. Oglesby, S. M. Day, Y.-G. Li, J. E. Vidale, *Bull. Seismol. Soc. Am.* **93**, 2459–2476 (2003).
11. H. S. Bhat, M. Olives, R. Dmowska, J. R. Rice, *J. Geophys. Res.* **112** (B11), B11309 (2007).
12. T. Ulrich, A.-A. Gabriel, J.-P. Ampuero, W. Xu, *Nat. Commun.* **10**, 1213 (2019).
13. R. Douilly, H. Aochi, E. Calais, A. Freed, *J. Geophys. Res. Solid Earth* **120**, 1108–1128 (2015).
14. S. Minson, M. Simons, J. Beck, *Geophys. J. Int.* **194**, 1701–1726 (2013).
15. K. Wang, D. S. Dreger, E. Tinti, R. Bürgmann, T. Taira, *Bull. Seismol. Soc. Am.* **110**, 1603–1626 (2020).
16. S. Barbot *et al.*, *Seismica* 10.26443/seismica.v2i3.502 (2023).
17. D. E. Goldberg *et al.*, *Seismic Record* **3**, 156–167 (2023).
18. V. Karabacak *et al.*, *J. Geol. Soc. London* **180**, jgs2023–jgs2020 (2023).
19. P. M. Mai *et al.*, *Seismic Record* **3**, 105–115 (2023).
20. D. Melgar *et al.*, *Seismica* 10.26443/seismica.v2i3.387 (2023).
21. R. Okuwaki, Y. Yagi, T. Taymaz, S. P. Hicks, *Geophys. Res. Lett.* **50**, e2023GL103480 (2023).
22. N. Lyberis, T. Yurur, J. Chorowicz, E. Kasapoglu, N. Gundogdu, *Tectonophysics* **204**, 1–15 (1992).
23. S. E. Güvercin, H. Karabulut, A. Ö. Konca, U. Doğan, S. Ergintav, *Geophys. J. Int.* **230**, 50–69 (2022).
24. T. Y. Duman, Ö. Emre, *Spec. Publ. Geol. Soc. Lond.* **372**, 495–529 (2013).
25. A. Koç, N. Kaymakcı, *J. Geodyn.* **65**, 292–307 (2013).
26. Materials and methods are available as supplementary materials.
27. Z. Jin, Y. Fialko, *Bull. Seismol. Soc. Am.* **110**, 1660–1679 (2020).
28. A. Lomax, Precise, NLL-SSST-coherence hypocenter catalog for the 2023 M_w 7.8 and M_w 7.6 SE Turkey earthquake sequence. *Zenodo* (2023); https://doi.org/10.5281/zenodo.8089273.
29. A. Doğru, F. Bulut, C. Yaltırak, B. Aktuğ, *Geophys. J. Int.* **224**, 389–400 (2021).
30. Z. Jia *et al.*, *Earth Planet. Sci. Lett.* **531**, 115997 (2020).
31. Z. Jia, Z. Zhan, H. Kanamori, *Geophys. Res. Lett.* **49**, e2021GL097104 (2022).
32. M. Ishii, P. M. Shearer, H. Houston, J. E. Vidale, *Nature* **435**, 933–936 (2005).
33. Z. Jia, X. Wang, Z. Zhan, *Geophys. Res. Lett.* **47**, e2020GL089802 (2020).
34. G. Ekström, M. Nettles, A. Dziewoński, *Phys. Earth Planet. Inter.* **200-201**, 1–9 (2012).

35. C. Liang, J. P. Ampuero, D. Pino Muñoz, *Geophys. Res. Lett.* **49**, e2022GL099749 (2022).
36. E. M. Dunham, *J. Geophys. Res. Solid Earth* **112**, JB004717 (2007).
37. E. Tinti *et al*., *Earth Planet. Sci. Lett.* **576**, 117237 (2021).
38. N. Kame, J. R. Rice, R. Dmowska, *J. Geophys. Res. Solid Earth* **108**, JB002189 (2003).
39. S. Fliss, H. S. Bhat, R. Dmowska, J. R. Rice, *J. Geophys. Res. Solid Earth* **110**, JB003368 (2005).
40. G. King, J. Nabecaronlek, *Science* **228**, 984–987 (1985).
41. D. Andrews, *J. Geophys. Res.* **94**, 9389–9397 (1989).
42. B. Duan, D. D. Oglesby, *J. Geophys. Res. Solid Earth* **112**, JB004443 (2007).
43. A. Rosakis, M. Abdelmeguid, A. Elbanna, Evidence of early supershear transition in the M_w 7.8 Kahramanmaraş earthquake from near-field records. arXiv:2302.07214 [physics.geo-ph] (2023).
44. S. S. Nalbant, J. McCloskey, S. Steacy, A. A. Barka, *Earth Planet. Sci. Lett.* **195**, 291–298 (2002).
45. Y. Fialko, *J. Geophys. Res. Solid Earth* **126**, e2021JB022000 (2021).
46. Z. Cakir *et al*., *Earth Planet. Sci. Lett.* **608**, 118085 (2023).
47. Y. Kaneko, Y. Fialko, D. T. Sandwell, X. Tong, M. Furuya, *J. Geophys. Res. Solid Earth* **118**, 316–331 (2013).
48. E. O. Lindsey, Y. Fialko, *J. Geophys. Res. Solid Earth* **121**, 1097–1113 (2016).
49. Y. Fialko, D. Sandwell, M. Simons, P. Rosen, *Nature* **435**, 295–299 (2005).
50. Z. Jin, Y. Fialko, *Geophys. Res. Lett.* **48**, e2021GL095213 (2021).
51. L. Dal Zilio, J.-P. Ampuero, *Commun. Earth Environ.* **4**, 71 (2023).
52. L. Luzi *et al*., *Bull. Earthquake Eng.* **18**, 5533–5551 (2020).
53. Disaster and Emergency Management Authority (AFAD) (1973); https://deprem.afad.gov.tr/event-catalog.
54. T. Taufiqurrahman *et al*., *Nature* **618**, 308–315 (2023).
55. S. Akkar, M. A. Sandıkkaya, J. J. Bommer, *Bull. Earthquake Eng.* **12**, 359–387 (2014).
56. Z. Jia *et al*, 2023_Turkey_doublet_Data_Model. Zenodo (2023); https://doi.org/10.5281/zenodo.8128343.

ACKNOWLEDGMENTS

We thank two anonymous reviewers for constructive comments. The facilities of IRIS Data Services, and specifically the IRIS Data Management Center, were used for access to waveforms, related metadata, and/or derived products used in this study. The GNSS data are provided by the General Directorate of Land Registry and Cadastre and the General Directorate of Mapping, Turkey. IRIS Data Services are funded through the Seismological Facilities for the Advancement of Geoscience (SAGE) Award of the National Science Foundation under Cooperative Support Agreement EAR-1851048. We thank the Engineering Strong-Motion (ESM) Database by ORFEUS (*52*) for providing access to the data from the Turkish National Strong Motion Network, which is operated by Turkey's Disaster and Emergency Management Authority (AFAD). The computations in this study were supported by the supercomputer SuperMUC-NG. **Funding:** Funding for this work was provided by the National Science Foundation (EAR-2123529, EAR-1841273 to Y.F., EAR-2022441, EAR-2143413 to W.F., and EAR-2121568 to A.-A.G), the National Aeronautics and Space Administration (80NSSC22K0506 to Y.F., 80NSSC20K0495 to A.A.G.), the United States Geological Survey (G22AP00011 to P.S. and W.F.), and the Cecil and Ida Green Foundation. M.M., T.U., and A.-A.G. were supported by the European Union's Horizon 2020 Research and Innovation Programme (TEAR grant 852992) and Horizon Europe (ChEESE-2P grant 101093038, DT-GEO grant 101058129, and Geo-INQUIRE grant 101058518). J.R. was supported by the National Science Foundation Graduate Research Fellowship Program (grant DGE-2038238). A.-A.G. gratefully acknowledges the Gauss Centre for Supercomputing e.V. (https://www.gauss-centre.eu) for providing computing time on the GCS Supercomputer SuperMUC-NG at Leibniz Supercomputing Centre (https://www.lrz.de), in project pn49ha. **Author contributions:** Z. Jia led the study, performed the subevent and kinematic slip inversions, and wrote the initial draft of the manuscript. Z. Jin, X.Z., and Y.F. processed the InSAR data, quantified the fault geometry, and performed static slip inversion. M.M., T.U., and A.-A.G. performed the dynamic rupture simulations and the Coulomb failure stress analysis. W.F. performed back projection analysis and coordinated the collaboration. Y.F. conducted static Coulomb stress calculations. X.Z. contributed to the fault geometry determination and figure design. J.R., T.U., and A.-A.G. conducted the ground motion analysis. F.B. and A.G. processed the GNSS data. W.F., P.S., A.-A.G., and Y.F. supervised the modeling and contributed to interpretation of the results. A.A.G., Y.F., and W.F. provided access to computational resources. All authors discussed the results and contributed to writing and revising the manuscript. **Competing interests:** The authors declare no competing interests. **Data and materials availability:** The Sentinel-1 SAR data are provided by the European Space Agency (ESA) and mirrored at the Alaska SAR Facility (ASF). The ALOS-2 PALSAR data are owned by the Japanese Space Agency (JAXA) and provided to Y.F. under a Research User Agreement. The global seismic data are publicly available from the IRIS-DMC. The regional strong motion data are publicly available from the EMS Database by ORFEUS. The geodetic and seismic data, the data-driven slip models and subevent models, and the data required to reproduce the dynamic rupture earthquake sequence scenarios can be downloaded from (*56*). We provide detailed README files summarizing the data and data formats provided.

SUPPLEMENTARY MATERIALS

science.org/doi/10.1126/science.adi0685
Materials and Methods
Figs. S1 to S28
Tables S1 and S2
References (*57–112*)
Movies S1 to S3

Submitted 1 April 2023; accepted 19 July 2023
Published online 3 August 2023
10.1126/science.adi0685

The complex dynamics of the 2023 Kahramanmara#, Turkey, M_W 7.8-7.7 earthquake doublet

Zhe Jia, Zeyu Jin, Mathilde Marchandon, Thomas Ulrich, Alice-Agnes Gabriel, Wenyuan Fan, Peter Shearer, Xiaoyu Zou, John Rekoske, Fatih Bulut, Asl Garagon, and Yuri Fialko

Science, **381** (6661), .
DOI: 10.1126/science.adi0685

Editor's summary
The Kahramanmara# earthquake sequence in Turkey on 6 February 2023 caused a tremendous amount of damage and loss of life. The sequence occurred across several faults, including and associated with the East Anatolian Fault, a strike-slip fault that has had many major earthquakes in the past. Jia *et al*. used an array of geophysical observations to produce models of how the ruptures occurred. The earthquake sequence ruptured at least six faults, including a large portion of the East Anatolian Fault. The rupture sequence was complex and contained surprises in the details of how the rupture occurred. These observations and models are important for understanding strike-slip faults and forecasting seismic hazards. —Brent Grocholski